PAPER

Check for updates

Nanoenzyme–chitosan hydrogel complex with cascade catalytic and self-reinforced antibacterial performance for accelerated healing of diabetic wounds†

Zhiguo Li,[a] Xiaotong Fan,[b] Zheng Luo,[a,c] Xian Jun Loh, [ID][c] Yedong Ma,[d] Enyi Ye, [ID][c] Yun-Long Wu, [ID] *[a] Chaobin He [ID] *[c,d] and Zibiao Li [ID] *[b,c,d]

The significant disability and fatality rate of diabetes chronic wounds necessitates the development of efficient diabetic wound healing techniques. The present oxygen treatments for wound healing is restricted by issues such as poor penetration, inadequate supply, and absorption difficulties as well as tanglesome diabetic wound microenvironment issues such as hyperglycemia, excessive reactive oxygen species (ROS), and hypoxia. Herein, we designed a multifunctional glucose oxidase (GOx) and catalase (CAT) nanoenzyme–chitosan (GCNC) hydrogel complex to improve the microenvironment of diabetic wounds and provide continuous oxygen delivery for efficient wound healing. By simultaneously forming the GOx–CAT nanoenzyme (GCNE) composite, the GCNC hydrogel complex could effectively reduce glucose and ROS (H_2O_2) concentrations in diabetic wounds through cascade catalytic reactions and achieve continuous oxygen supply, which promoted cell proliferation, migration, and angiogenesis, thereby accelerating diabetic wound healing. In addition, the byproduct gluconic acid produced by the cascade reaction can activate the amino group of chitosan to reinforce the antibacterial performance and prevent microbial infection. This multifunctional GCNC hydrogel complex with continuous oxygen supply, self-reinforcing antibacterial properties, and byproduct-free features provides a general strategy for repairing the extensive tissue damage in diabetes.

1. Introduction

Diabetes is one of the most critical public health concerns impacting human health in the 21st century. It has been on the rise in the last ten years, and it is anticipated to affect 10% of the world's population by 2030.[1,2] Currently, more than 25% of diabetes patients are in danger of amputation, such as diabetic foot, or possibly death owing to chronic non-healing wounds. Ordinary wound healing requires the precise coordination and integration of complicated biological and molecular activities such as cell migration, proliferation, extracellular matrix deposition, and angiogenesis.[3–5] However, diabetic wounds are typically difficult to heal fast and efficiently owing to the complicated physiological milieu of diabetic wounds, such as tissue hypoxia, hyperglycemia, and oxidative stress and are often vulnerable to pathogenic bacteria that aggravate the condition.[6–9] To speed the healing of chronic diabetes wounds, a novel technique that can cope with the intricate physiological milieu of diabetic wounds is required.

Oxygen is essential for wound healing because it can effectively promote cell proliferation, metastasis and angiogenesis, and other wound repair processes.[10–13] Currently, hyperbaric therapy and local gaseous oxygen therapy have been used to treat diabetes in clinics.[12,14–16] However, because their oxygen supply is gaseous oxygen, they encounter issues such as low tissue permeability, and difficulties delivering and sustaining effective oxygen concentrations, resulting in inadequate therapy outcomes.[17–22] In recent years, researchers have investigated a variety of oxygen delivery strategies to ensure effective oxygen delivery in wounds, including supplying oxygen-binding hemoglobin[23,24] or photosynthetic algae organisms[25,26]

[a] *Fujian Provincial Key Laboratory of Innovative Drug Target Research and State Key Laboratory of Cellular Stress Biology, School of Pharmaceutical Sciences, Xiamen University, Xiamen 361102, China. E-mail: wuyl@xmu.edu.cn*

[b] *Institute of Sustainability for Chemicals, Energy and Environment (ISCE²), Agency for Science, Technology and Research (A*STAR), 2 Fusionopolis Way, 138634 Singapore. E-mail: lizb@imre.a-star.edu.sg*

[c] *Institute of Materials Research and Engineering, A*STAR (Agency for Science, Technology and Research); 2 Fusionopolis Way, Innovis, #08-03, Singapore 138634, Singapore*

[d] *Department of Materials Science and Engineering, National University of Singapore, 9 Engineering Drive 1, Singapore 117576, Singapore. E-mail: msehc@nus.edu.sg*

that can dramatically expedite wound healing.[23,25,27–29] Despite the fact that these treatments have effectively enhanced the oxygen flow to the wound, the high-efficiency and continuous provision of oxygen still confronts significant obstacles due to the complicated physiological milieu of diabetes. Besides hypoxia, adverse hyperglycemia and an oxidative microenvironment (such as high H_2O_2) slow diabetic wound healing.[4,30,31] As a result, developing a technique for diabetic wound recovery that can effectively regulate blood sugar, reduce ROS (such as H_2O_2), and constantly deliver oxygen is very desirable.

In recent years, enzymes and their analogues have shown considerable promise in speeding wound healing.[32–38] A variety of wound dressings containing enzyme or enzyme-like abilities are being developed to catalyze endogenous H_2O_2 at the wound site, generating oxygen and improving the diabetic microenvironment,[39,40] such as catalase-like polyvinyl alcohol film with hematite[38] or multifunctional hydrogel containing manganese dioxide.[37] It has been shown that improving the imbalanced physiological environment in diabetic wounds and increasing oxygen delivery are effective strategies for treating significant tissue damage caused by diabetes. However, it is challenging to create and maintain adequate oxygen concentration at the wound owing to insufficient endogenous H_2O_2 and the restricted enzymatic activity of individual nanozymes. Because of its high local concentration, reduced intermediate decomposition, and high mass transfer efficiency, the enzyme cascade reaction in biological systems can significantly improve catalytic performance.[41] For example, the glucose oxidase (GOx) and catalase (CAT) cascade systems have been investigated in the treatment of diabetic wounds,[42–45] with GOx primarily consumes glucose to create H_2O_2, while CAT further catalyzes H_2O_2 to provide sufficient oxygen. However, the majority of these systems use metal or metal oxide enzyme-like compounds, and their catalytic effectiveness, the cascade effect, and safety of byproducts such as acid or metal ions are all causes for concern. It is critical for the construction of a safe and efficient enzyme cascade system to understand how to increase enzyme stability, the cascade efficiency, and decrease unwanted by-products via rational material design. Natural enzymes have excellent cascade catalytic efficiency as well as biocompatibility. Hydrogels have high water content and cargo loading efficiency, as well as superior biocompatibility, making them popular in wound healing applications.[46–49]

Herein, we designed an injectable GOx–CAT nanoenzyme–chitosan (GCNC) hydrogel system for wound healing in diabetes mellitus, as shown in Scheme 1. GOx–CAT nanoenzyme (GCNE) composites were prepared by polymerization using acryloxylated GOx and CAT, acrylamide (AAm), and N,N′-methylenebisacrylamide (BIS). Due to the close spatial distance between GOx and CAT, H_2O_2 generated after GOx catalyzes glucose in diabetic wounds and endogenous H_2O_2 can be rapidly catalyzed by CAT to produce O_2. Meanwhile, the generated O_2 can in turn improve the catalytic activity of GOx, allowing it to efficiently regulate blood glucose while continually producing O_2. In addition, the gluconic acid catalyzed by the GOx catalytic reaction can activate the amino groups of chitosan in the hydrogel, which further improves the antibacterial activity of chitosan while consuming acidic by-product gluconic acid. To the best of our knowledge, this multi-functional diabetic wound dressing hydrogel is described for the first time with multiple functions of controlling blood glucose, antibacterial, hemostasis, improving the oxidative microenvironment of the diabetic wound, and circulating oxygen supply, demonstrating a versatile strategy for healing a broad range of tissue damage caused by diabetes.

2. Results and discussion

2.1. Synthesis and characterization of multifunctional GOx–CAT nanoenzyme–chitosan (GCNC) hydrogel system

The GOx–CAT nanoenzyme and chitosan-modified injectable hydrogel were physically mixed to obtain a multifunctional GOx–CAT nanoenzyme–chitosan (GCNC) hydrogel complex system (Scheme 1).[50,51] TEM was used to observe the morphology of the nanoenzyme composite. As shown in Fig. 1A, the spherical structure with a size of about 90 nm is clearly visible, and the DLS image also shows that the average particle size is about 128 nm, which is attributed to the water swelling ability of nanoenzyme. Besides, SEM was used to observe the morphology of the GCNC hydrogel complex. As shown in Fig. 1B, the hydrogel structure of the porous network is clearly visible, facilitating the delivery of oxygen and nutrients. The injectable and adhesive properties of the GCNC hydrogel
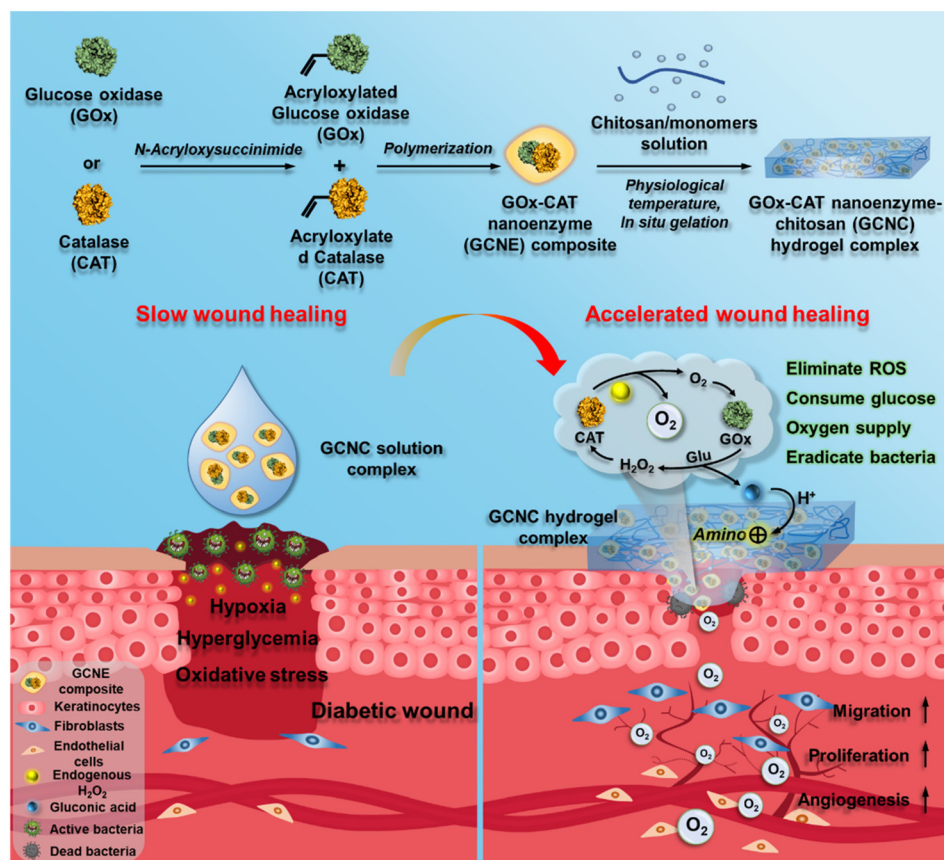
Zibiao Li

*Dr Zibiao Li is the Director of the Sustainable Polymers Division at Institute of Sustainability for Chemicals, Energy and Environment (ISCE²), A*STAR, Singapore. Li holds a joint appointment at the Institute of Materials Research and Engineering (IMRE) and is an adjunct Associate Professor at the National University of Singapore (NUS). His research interests focus on material sustainability and MedTech polymers for healthcare applications. He has more than 200 publications in the interdisciplinary field of nanomaterials and polymers. Recently, he served as a guest editor for the themed collection of "Flexible nanomaterials" with* Nanoscale Advances *and edited two books entitled* Sustainable Nanotechnology *and* Photothermal Nanomaterials *in Nanoscience & Nanotechnology Book Series published by RSC. So far, he has 43 publications with RSC, including articles published in* Chem. Soc. Rev.*,* J. Mater. Chem. A, B, C*;* Nanoscale*, and* Green Chem.

Scheme 1 The design of GOx–CAT nanoenzyme–chitosan (GCNC) hydrogel complex with cascade catalytic and self-reinforced antibacterial performance for accelerated healing of diabetic wounds.

complex are also shown in Fig. S1D.† When at room temperature, the hydrogel is in a liquid state; when at 37° C, the hydrogel solidified, which illustrates the thermos-sensitive properties of the hydrogel. Then, the stability of the GCNC hydrogel complex was evaluated. As shown in Fig. S1A,† the GCNC hydrogel complex under PBS and the acidic, oxidative, and glucose-containing microenvironment remained stable (weight remained above 80%) within 48 h. The weight of hydrogel was monitored, as shown in Fig. S1B.† The weight showed a slight decrease, which may be due to the degradation and release behavior of hydrogels. Importantly, the slow release behavior of the GCNC hydrogel complex was evaluated, as shown in Fig. 1C. In solution 1 (PBS), the protein amount of hydrogel released was less than that in solution 2 (PBS containing glucose, acid, and H_2O_2), which may be due to the faster degradation of hydrogels in solution 2.

After the characterization of hydrogels, it is vital to demonstrate the cascade catalytic activity of the GOx–CAT nanoenzyme (GCNE) composite. Due to the close spatial distance of both enzymes in the nanostructure, GCNE composite can have an efficient enzyme cascade reaction, thus generating a large amount of oxygen through cyclic catalysis. Firstly, glucose (Glu) can be catalyzed by GOx to produce H_2O_2 and gluconic acid. Therefore, the pH value of the solution should decrease

with the progress of the reaction. As shown in Fig. 1D, the reaction between Glu and GCNE composite proceeded quickly in a short time as the pH decreased from 7 to about 3.2 within 10 h and remained stable. However, the pH values of other groups were almost unchanged (maintaining between 6 and 7), which verified the catalytic reaction of GOx in the presence of Glu. Secondly, H_2O_2 can be catalyzed by CAT to produce oxygen and water, so the production of oxygen symbolizes the progress of the CAT reaction. As shown in Fig. 1E, a large number of bubbles were generated at the moment when 30% H_2O_2 reacted with the GCNE composite, and the concentration of dissolved oxygen (DO) in the solution increased rapidly from 5 up to 35 mg L^{-1} within 30 s. However, the DO concentration of other groups was almost unchanged (kept around 5 mg L^{-1}), which verified the catalytic reaction of CAT in the presence of H_2O_2. The above results indicate that the catalytic performance of the two enzymes in the nanostructure was still effective and not affected by polymerization. In addition, in order to verify the cascade catalytic effect of the GCNE composite, we placed it in a solution containing only Glu. As shown in Fig. 1F, we can see that compared with single-GOx nanoenzyme materials, the GCNE composite could effectively regulate the rate of oxygen concentration reduction, because CAT in the GCNE composite could catalyze H_2O_2 to produce O_2. Finally,

Fig. 1 (A) The representative TEM image and particle size of GOx−CAT nanoenzyme (GCNE) composite. Scale bar, 100 nm. (B) The representative SEM image and gelation photographs of GOx−CAT nanoenzyme−chitosan (GCNC) hydrogel complex. Scale bar, 5 μm. (C) Protein release property evaluation of GCNC hydrogel complex under (1) PBS and (2) the solution with glucose, acid, and H_2O_2. (D) Schematic and evaluation of GOx activity: change in pH after the reaction of GCNE composite with glucose. (E) Schematic and evaluation of CAT activity: dissolved oxygen concentration after GCNE composite reaction with hydrogen peroxide. (F) Cascade reaction activity of GCNE composite: change in dissolved oxygen concentration after the reaction with glucose. (G) Change in dissolved oxygen concentration after GCNE composite treatment under simulated diabetic wound environment with high glucose and oxidative stress *in vitro*. Error bars represent mean ± s.d. ($n = 3$, ***$p < 0.001$, **$p < 0.01$, *$p < 0.05$).

we used Glu and H_2O_2 to mimic the conditions of high glucose and high oxidative stress in diabetic wounds, so as to evaluate the catalytic reaction of the GCNE composite. Because the glucose oxidation reaction consumes oxygen, CAT is required to consume endogenous H_2O_2 at the wound site to produce oxygen. With the production and consumption of H_2O_2, oxygen production gradually increases. As shown in Fig. 1G, DO can rise rapidly to 10.6 mg ml^{-1} within 4 minutes because a large amount of oxygen was produced by the decomposition of H_2O_2. In the next two minutes, the oxygen concentration decreased slightly and remained at about 9.9 mg mL^{-1}, which is due to the excellent catalytic ability of the GCNE composite. Last but not least, the oxygen supply ability of the GCNC hydrogel complex was also evaluated. As shown in Fig. S1C,† after adding 30% H_2O_2 into the GCNC hydrogel complex, a large number of bubbles were generated

instantaneously, which showed that the GCNC hydrogel complex still retains good catalytic activity of the GCNE composite. Overall, the as-designed GCNE composite possesses good catalytic activity, and it can continuously generate oxygen through a cascade catalytic reaction in the presence of glucose.

2.2. H$^+$ absorption effect of the GCNC hydrogel complex

The cytotoxicity of the GCNE composite on cell lines was tested by MTT assays. As shown in Fig. 2A and B, the GCNE composite showed the ability to promote growth at low concentrations, but with the increase in concentration, cell activity gradually decreased, which may be caused by the gluconic acid byproduct produced by GOx. Considering that gluconic acid catalyzed by GOx will produce acidic conditions in the wound, which has a negative effect on the wound healing process by reducing pH in the environment; we chose chitosan-based
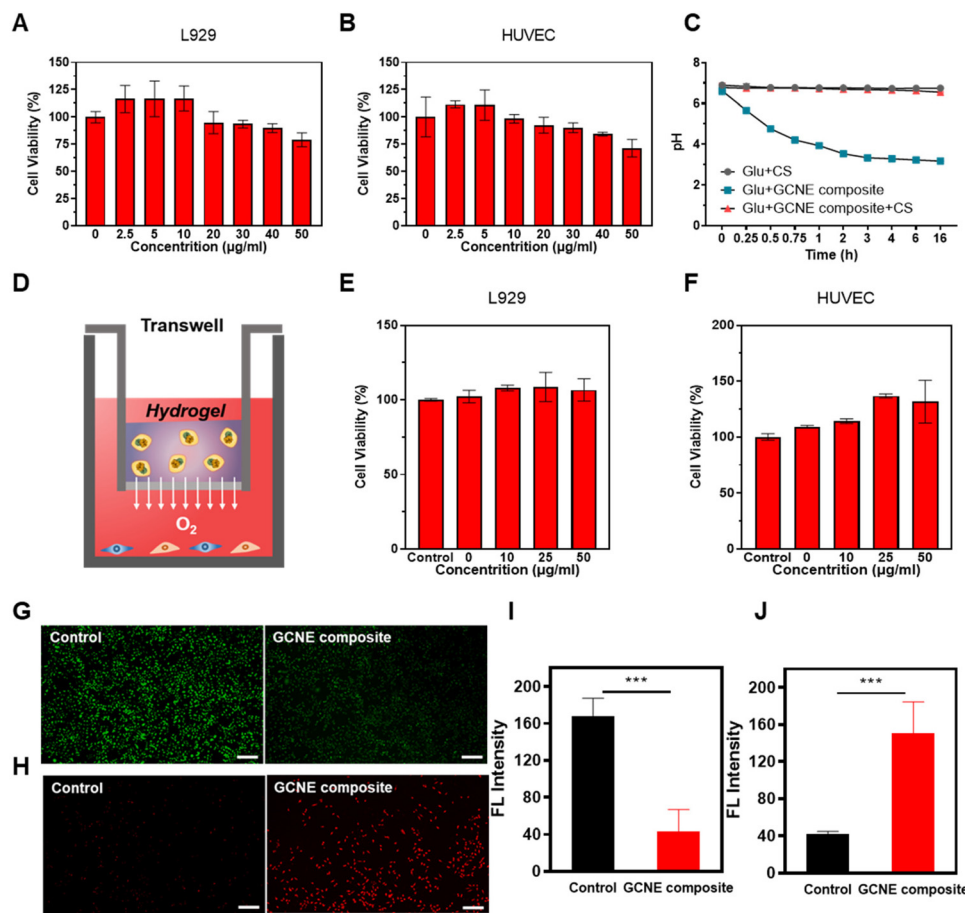
Fig. 2 The cell viability of (A) L929 cells and (B) HUVECs treated with GCNE composite for 24 h based on MTT assay. (C) Effect of chitosan on pH of GCNE composite reaction solution. (D) The schematic diagram of GCNC hydrogel complex toxicity test on (E) L929 cells and (F) HUVECs. (G) Representative images showing the alleviation of oxidative stress in L929 cells treated with H_2O_2 and H_2O_2 + GCNE composite monitored *via* a ROS probe (DCFH-DA). Scale bars, 200 μm. (H) Representative images of intracellular O_2 generation after FBS-free DMEM and GCNE composite treatment of L929 cells, validated by the O_2 probe $[Ru(dpp)_3]Cl_2$. Scale bars, 200 μm. (I and J) The quantitative studies of ROS depletion and O_2 generation, respectively, in L929 cells and the fluorescence intensity, were quantified using ImageJ software (n = 3). Error bars represent mean ± s.d. (n = 3, ***$p < 0.001$, **$p < 0.01$, *$p < 0.05$).

(CS) hydrogel to attenuate this effect. Since chitosan has many amino groups, it has the function of adsorbing H^+, so under the action of chitosan, the pH of the mixed solution of GCNE composite and Glu will decrease more slowly. Meanwhile, it can enhance the antibacterial effect of chitosan due to the positive charges. As shown in Fig. 2C, we found that the pH value of the mixed solution of Glu and GCNE composite could be reduced from 6.62 to about 3.18 in 16 h, but the addition of chitosan could significantly slow down this decline, and its pH value was maintained at about 6.7. Then, the cytotoxicity of the GCNC hydrogel complex was studied, as illustrated in Fig. 2D. As shown in Fig. 2E and F, the GCNE composite did not decrease the cell activity at high concentrations because of chitosan-based hydrogel-adsorbed H^+ and avoided the decline of the environmental pH. Therefore, chitosan can avoid the adverse effect of excessive acid on wound healing, while improving the antibacterial properties to promote the process of wound healing.

2.3. Anti-oxidative stress and oxygen supply effect of GCNE composite

The above results prove that the GCNE composite had good *in vitro* oxygen-release performance, so it is of great significance to explore the effects of nanoenzyme, intracellularly. Wounds have been reported to be in a state of oxidative stress due to increased production of ROS (H_2O_2), leading to wound damage. We hypothesized that the GCNE composite could mitigate this oxidative environment because CAT could deplete H_2O_2. The ROS probe DCFH-DA was employed to detect the intracellular ROS level after L929 cells were placed into a state of oxidative stress by H_2O_2 and treated with the GCNE composite, the result of which illustrated the good ROS depletion ability of the GCNE composite (Fig. 2G and I). In addition, the intracellular oxygen level was detected to verify the O_2-release ability of the GCNE composite by using an oxygen probe, $[Ru(dpp)_3]Cl_2$. After the treatment, the intracellular fluorescence

intensity of L929 cells increased significantly (Fig. 2H and J), indicating that the oxygen produced by the GCNE composite can effectively increase the oxygen supply in the cell.

2.4. Promotion of proliferation, migration, and angiogenesis of the GCNE composite *in vitro*

In the process of wound healing, many cells such as endothelial cells and fibroblasts, play an extremely important role in neovascularization and tissue formation. However, their life activities are inhibited by hypoxic and oxidative stress conditions of the wound site. Therefore, L929 cells and HUVECs cells pretreated with H_2O_2 were selected as model cells to verify the effects of continuous oxygen production by the GCNE composite on cell migration and proliferation. Firstly, we evaluated the promoting effect of the GCNE composite on cell proliferation using CFSE-staining. As shown in Fig. 3A and B, the fluorescence intensity of GCNE composite-treated L929 cells gradually weakened from 201.32 AU down to 55.53 AU within 72 h, while the control group weakened from 200.83 AU down to 106.04 AU. As shown in Fig. 3C and D, the fluorescence intensity of GCNE composite-treated HUVECs gradually weakened from 185.30 AU down to 49.60 AU within 72 h, while the control group weakened from 178.08 AU down to 104.76 AU. The decrease in the fluorescence intensity indicates cell division, illustrating that the oxygen produced in the glucose-containing medium can promote cell proliferation.

Generally, endothelial cells and fibroblasts contribute to tissue formation and re-epithelialization during the proliferation stage of the wound healing process. Therefore, the effect of oxygen produced by the GCNE composite on the migration of L929 and HUVECs pretreated with H_2O_2 was investigated through *in vitro* wound-healing assay. As shown in Fig. 3E–H, the cell migration rates of L929 cells and HUVECs cells within 12 h were 38.37% and 74.12%, respectively. Compared with the control group (L929 13.06%; HUVECs 25.8%), the GCNE composite can significantly promote the migration of cells ($p < 0.05$), which demonstrated that the oxygen produced from the GCNE composite could promote wound healing by promoting epithelialization.

In addition, endothelial cells were found to play an essential role in vascular function and angiogenesis. Thus, a matrigel tube formation assay was carried out to evaluate the capability of angiogenesis, which showed that the tube length and branch points of HUVECs after 4 h treatment were significantly higher in the GCNE composite-treated HUVECs than those in the control group, and the grid structure was also shown in the visualization (Fig. 3I–K). These consequences suggested that the enhanced vessel-forming ability revealed that a good deal of *in vitro* assays was due to the production of oxygen by the GCNE composite.

The above experiments show that the GCNE composite could alleviate intracellular oxidative stress and supply sufficient oxygen to cells such as L929 cells and HUVECs, which are active in the wound healing process, resulting in accelerating the process of tissue formation and re-epithelization. Moreover, it can also use the amino group in the chitosan hydrogel to adsorb hydrogen ions to avoid the change in pH of

the wound microenvironment caused by the byproduct gluconic acid, so as to reduce or eliminate the adverse effects brought by the byproduct.

2.5. Antibacterial activity of GCNC hydrogel complex

Bacterial infection is considered to be a major obstacle to the healing process of diabetic wounds. Therefore, the antibacterial behavior of chitosan-based hydrogel was comprehensively estimated *in vitro*. Gram-positive *S. A* and Gram-negative *E. coli* were used as model bacteria to conduct antibacterial experiments. As illustrated in Fig. 4A and B, we found the viability of bacteria in the Glu group was higher than that in the Control group ($p < 0.05$), which means the high glucose environment is conducive to the growth of bacteria. Expectantly, our chitosan-based hydrogel showed good antibacterial activity against *S. A* and *E. coli*. According to our results, the relative viability of Glu + CS hydrogel-treated *S. A* and Glu + GCNC hydrogel complex-treated *S. A*, respectively, reached only 12.89% and 5.25% ($p < 0.05$). Besides, the relative viability of the Glu + CS hydrogel-treated *E. coli* and Glu + GCNC hydrogel complex treated *E. coli*, respectively, reached only 31.98% and 22.18% ($p < 0.05$). These results were because the chitosan-adsorbed H^+ was produced by the by-product gluconic acid according to our previous experiments (Fig. 2C), which enhanced the positive charge of chitosan and thus enhanced the antibacterial effect. The results of the visual antibacterial images were consistent with the above findings (Fig. 4C). We could observe that there were a large number of colony formations in the group control, Glu and Glu + GCNE composite. On the contrary, the hydrogel groups had a small colony formation. Overall, the excellent antibacterial property of the GCNC hydrogel complex could provide a protective barrier for wound healing.

2.6. GCNC hydrogel complex accelerates diabetic chronic wound healing *in vivo*

In order to further verify the effect of the GOx–CAT nanoenzyme (GCNE) composite in accelerating diabetic wound healing *in vivo*, we established a chronic wound model of *Staphylococcus aureus* (*S.A*) infection in diabetic SD rats for verification (Fig. 5A). The blood glucose of the tail vein was monitored to ensure the rats were in a hyperglycemic state (always higher than 16.7 mmol ml^{-1}; Fig. 5B). In addition, we randomly measured the blood glucose values of the wound site in healthy and diabetic rats, the results of which showed that the wound in diabetic mice was also a high glucose environment (Fig. S2†).

Digital photographs of the wounds showed that the wound healing rates of *S. A* + hydrogel, *S. A* + GCNE composite, and *S. A* + GCNC hydrogel complex groups were faster than that of the control (73.94%) and *S. A* group (69.09%), with 74.81%, 82.59%, and 92.68% closure area, respectively (Fig. 5C–F). In order to observe the organizational characteristics after *in vivo* wound healing assay, a detailed histomorphological study was also performed by hematoxylin and eosin (H&E) staining (Fig. 5G). The size of skin wounds in each group could also be clearly observed from the tissue section diagram. The size of skin wounds in the *S. A* group was obviously bigger than that

Fig. 3 The effect of the GCNE composite response on cell activity. (A and B) Representative fluorescence images of L929 cell proliferation staining with CFSE at different time points (n = 3) and the fluorescence intensity were quantified using ImageJ software. Scale bars, 200 μm. (C and D) Representative fluorescent images of HUVECs proliferation stained with CFSE at different time points (n = 3) and the fluorescence intensity was quantified using ImageJ software. (E and F) Representative images of L929 cell migration within 12 h and quantitative analysis calculated using ImageJ software (n = 3). Scale bars, 200 μm. (G and H) Representative images of HUVECs migration within 12 h and quantitative analysis calculated using ImageJ software (n = 3). Scale bars, 200 μm. (I, J, and K) Representative images of HUVECs' tube formation and quantitative analysis calculated by ImageJ software (n = 3). Scale bars, 200 μm. Error bars represent mean $\pm$ s.d. (n = 3, ***p < 0.001, **p < 0.01, *p < 0.05).

in the other groups, while wounds observed in the *S. A* + GCNC hydrogel complex group had already healed (black dotted line). Besides, *S. A* infection was observed to affect hair follicle growth (blue arrow), but hair follicles continued to grow normally on the skin treated with the hydrogel and GCNE composite. Furthermore, a large number of blood vessels were observed in the *S. A* + GCNE composite and *S. A* + GCNC hydrogel complex groups (red arrow), owing to oxygen production by the GCNE composite at the wound site. During the remodeling phase, proper collagen deposition is important to promote wound healing. Therefore, Masson's trichrome staining was performed to observe newly formed collagen

(Fig. S3†). The results showed that the *S. A* + GCNE composite and *S. A* + GCNC hydrogel complex group had more collagen deposition (blue). These results are attributed to the fact that the GCNE composite can generate oxygen by utilizing blood glucose in the microenvironment to promote the physiological functions of various cells, such as enhanced cell proliferation, migration, and angiogenesis, resulting in accelerating wound healing in diabetic wounds.

To verify the *in vivo* antibacterial effect of the GCNC hydrogel complex, the skin tissue homogenate was used for LB agar plate coating, and the results showed that *S. A* + CS hydrogel and *S. A* + GCNC hydrogel complex group had better *in vivo*
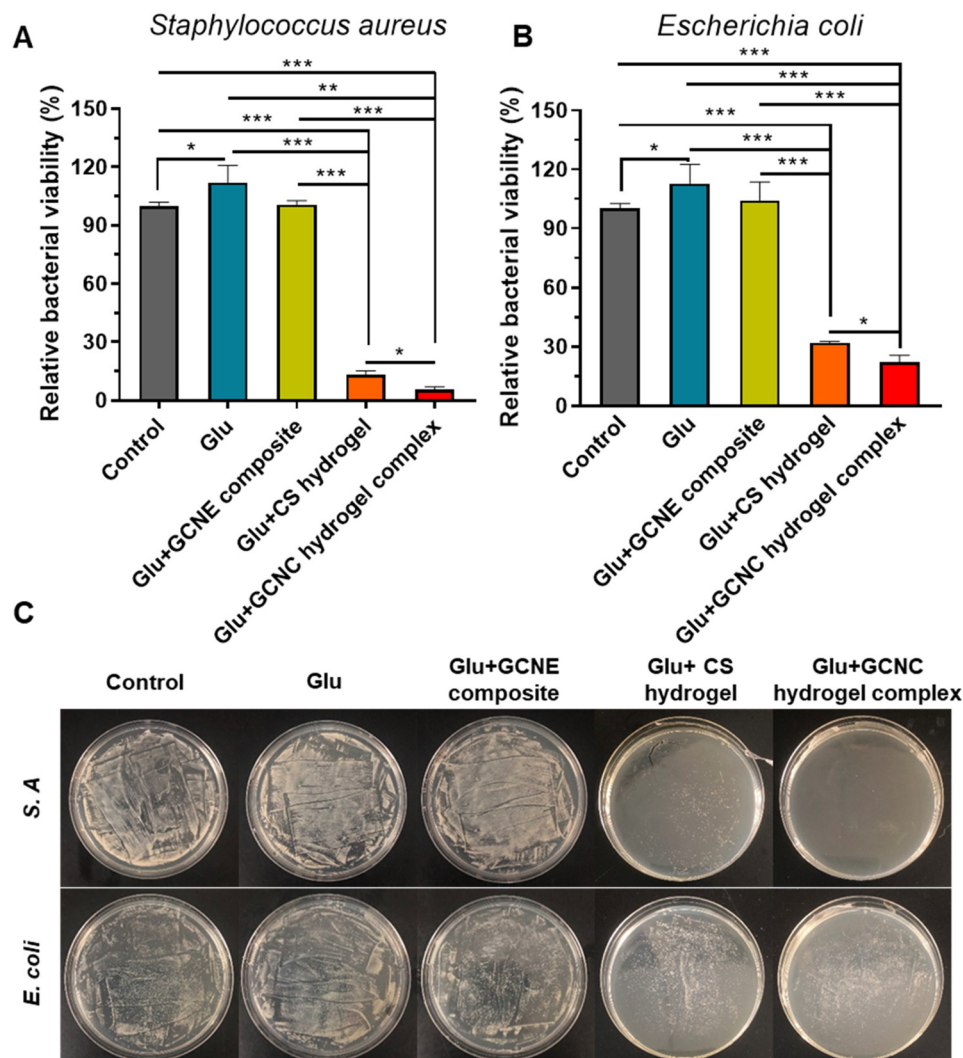
Fig. 4 Evaluation of the antibacterial activity of the GCNC hydrogel complex. (A) Quantitative analysis of inhibition by chitosan-based hydrogel towards *Staphylococcus aureus*. (B) Quantitative analysis of inhibition by chitosan-based hydrogel towards *Escherichia coli*. (C) Representative images of visual bacteria clones on LB agar surface with different treatments. Error bars represent mean ± s.d. ($n = 5$, ***$p < 0.001$, **$p < 0.01$, *$p < 0.05$).

antibacterial effect (Fig. S4†). Additionally, in order to explore the biological safety of the system, we monitored the weight changes of rats and performed a frozen section analysis on their main tissues and organs. From Fig. 5E, it can be seen that the GOx–CAT nanoenzyme (GCNE) composite did not show a significant effect on the body weight of the rat, and the H&E staining analysis (Fig. S5†) did not demonstrate any pathological changes in the main organs of the rat, indicating that the system has good biocompatibility and no obvious toxicity.

2.7. Oxidative stress depletion and angiogenesis effect of the GCNC hydrogel complex *in vivo*

We detected the elimination of ROS in tissue sections to verify the *in vivo* alleviation of wound oxidative stress. As shown in Fig. 6A and B, the results showed lower fluorescence in the GCNE composite group than that in other groups, demonstrating that the GCNE composite could effectively eliminate ROS

at the wound and alleviate oxidative stress. In addition, neovascularization was observed by CD31 immunostaining (Fig. 6C and D). There was a large amount of red fluorescence in the *S. A* + GCNE composite and *S. A* + GCNC hydrogel complex groups, which was significantly higher than that in other groups, indicating many new blood vessels, which provided stimulative factors to accelerate wound healing. Overall, by simultaneously eliminating oxidative stress, supplying oxygen, and facilitating angiogenesis, our GCNC hydrogel complex significantly accelerated the wound closure rate.

3. Materials and methods

3.1. Materials

Chitosan (deacetylation value 75.0 to 85.0%) was purchased from Shanghai Aladdin Biochemical Technology Co., Ltd.
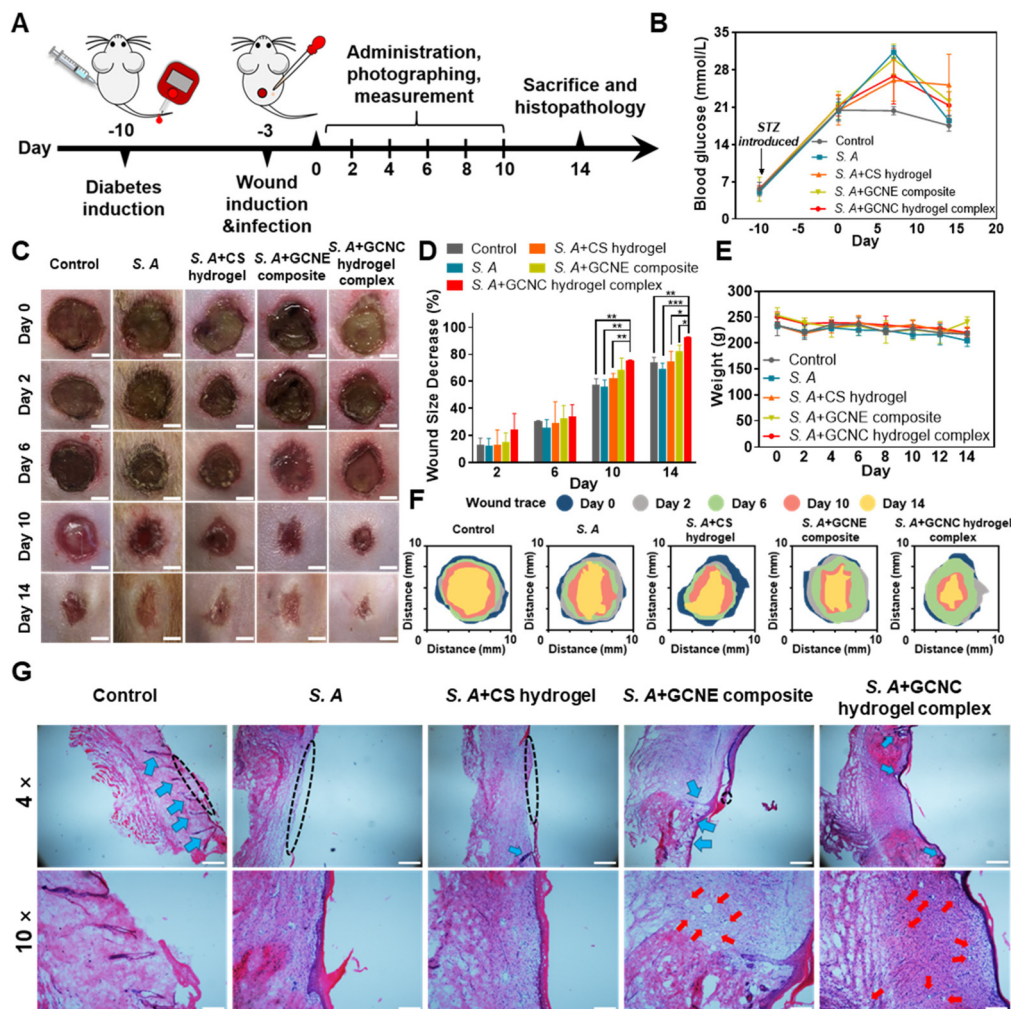
Fig. 5 The GCNC hydrogel complex promotes diabetic wound healing *in vivo* by providing oxygen and inhibiting bacteria. (A) Schematic diagram illustrating the timeline and operation of animal experiments. (B) The changes in blood glucose in all diabetic rats were monitored during the whole animal experiment. (C) Representative images of the wound healing process of diabetic rats with different treatments at different time points. Scale bars, 0.25 cm. (D) Quantitative analysis of the wound size decrease rate of 5 groups at different time points. (E) Changes in the body weight of all diabetic rats were monitored throughout the experiment. (F) Traces of wound-bed closure during animal experiments made by PowerPoint software. (G) Histomorphological evaluation of wound regeneration by H&E staining under two kinds of magnifications (dotted line, unhealed wound; red arrow, blood vessels; blue arrow, hair follicles). Scale bars of 4× images, 500 μm; scale bars of 10× images, 200 μm. Error bars represent mean $\pm$ s.d. ($n = 5$, ***$p < 0.001$, **$p < 0.01$, *$p < 0.05$).

Phosphate-buffered solution (PBS) was supplied by Beyotime Biotechnology Co., Ltd. Biological materials included D-glucose, anhydrous (Solarbio), yeast extract powder (OXOID), tryptone (OXOID), agar powder (Solarbio), Dulbecco's Modified Eagle's Medium (DMEM, Gibco), Endothelial Cell Medium (ECM) containing 500 ml basalmedium, 25 ml FBS, 5 ml endothelial cell growth supplement and 5 ml antibiotic solution (ScienCell), penicillin–streptomycin (Yeasen), fetal bovine serum (FBS; Thermo Fisher Scientific), Matrigel Matrix Basement Membrane (BD Biosciences), Hematoxylin and Eosin Staining Kit (Yeasen), tris (4,7-diphenyl-1,10-phenanthroline) ruthenium(II) dichloride complex ([Ru(dpp)₃]Cl₂, CAS 36309-88-3), DCFH-DA (Beyotime Biotechnology) DAPI-containing sealant (Yeasen) and 3-(4,5-dimethyl-2-thiazolyl)-2,5-diphenyl-2-*H*-tetrazolium bromide (MTT; Yeasen). Equipment included a blood glucose meter (Sinocare Inc.), JPB-607A portable dissolved oxygen tester (Shanghai INESA Scientific Instrument Co., Ltd), and PHS-3C pH meter (Shanghai INESA Scientific Instrument Co., Ltd). The instruments used in the experiment were all from the Core Facility of Biomedical Sciences, Xiamen University.

3.2. Characterization of GCNE composite

The GCNE composite and (chitosan-*g*-poly (*N*-isopropylacrylamide) [CS-*g*-PNIPAAM]) hydrogel were synthesized according to our previous research. The GCNC hydrogel complex was formed by physically mixing 5% w/v chitosan-based hydrogel with the GCNE composite. A transmission elec-
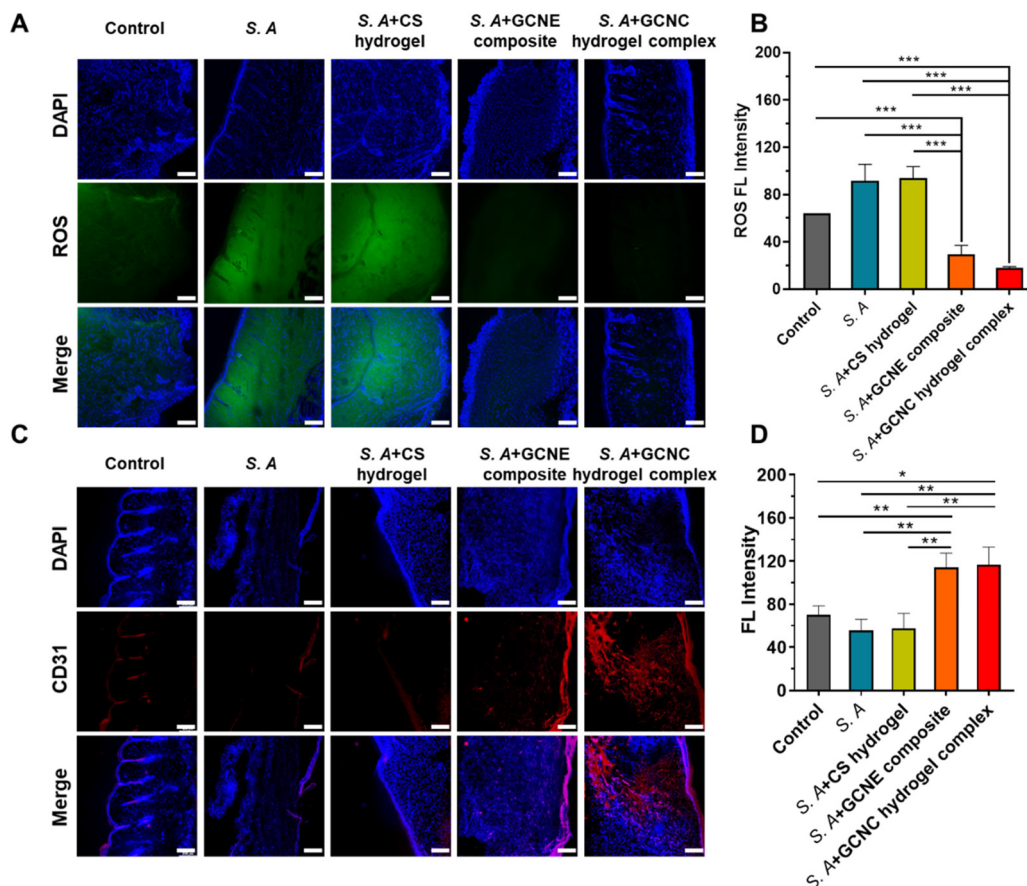
Fig. 6 (A) Representative fluorescence images of ROS levels with DHE staining (green) and DAPI (blue). Scale bars, 200 μm. (B) The relative fluorescence intensity of ROS was quantified using ImageJ software (n = 3). (C) Representative immunofluorescence images of flaps highlighting blood vessel CD31-positive endothelial cells (red) and DAPI (blue). Scale bars, 200 μm. (D) The relative fluorescence intensity of CD31 was quantified using ImageJ software (n = 3). Error bars represent mean ± s.d. (n = 3, ***p < 0.001, **p < 0.01, *p < 0.05).

tron microscope (TEM) was used to observe the samples. Sample pretreatment: the sample was weighted and dissolved in a small volume of double distilled water (dd water), then it was added to the total volume of double distilled water dropwise while stirring (the final concentration 1 mg ml^{-1}), stirring it overnight. 10 μl of it was dropped onto the 400 mesh copper wire and kept for adsorption (10 min). A scanning electron microscope (SEM) was used to observe the hydrogel. The sample was pre-treated to gel and the powder on the surface was blown clean before being tested. Dynamic light scattering (DLS) measurements were conducted to investigate the size of the GCNE composite. For the injectability, adhesion, and stability of the hydrogel, 5% w/v chitosan-based hydrogel containing 1 mg ml^{-1} GCNE composite was used. Two solutions (PBS and pH = 5 PBS containing 3 mg ml^{-1} glucose, 3 mM H$_2$O$_2$, and acetic acid) were added to the hydrogel, then the hydrogels were weighed at different time points.

The cumulative release of protein was detected by the BCA assay kit (SparkJade). 5% w/v chitosan-based hydrogel containing 2 mg ml^{-1} GCNE composite was used. Two groups were tested: (1) GCNC hydrogel complex + PBS; (2) GCNC hydrogel complex + pH = 5 PBS containing 3 mg ml^{-1} glucose, 3 mM

H$_2$O$_2$ and acetic acid. When tested, solution (2) was used as a control to eliminate the interference of the solvent.

3.3.   *In vitro* reactivity evaluation of GCNE composite

Measurement of pH: different groups (dd water, Glu, GCNE composite, Glu + GCNE composite) were placed in a 37 °C incubator and their pH values were measured at different time points. The glucose concentration was 3 mg ml^{-1}, and all the GCNE composite concentrations in this article are referred to GOx, which is 25 μg ml^{-1}. The measurement of dissolved oxygen (DO): in order to verify the reaction activity of CAT and the reaction activity of the whole system, three groups of experiments were set up. The first group included dd water, 30% H$_2$O$_2$, GCNE composite, and 30% H$_2$O$_2$ + GCNE composite. The second group includes Glu, GCNE composite, GOx, Glu + GOx, and Glu + GCNE composite. The third group includes Glu + 250 μM H$_2$O$_2$, Glu + 250 μM H$_2$O$_2$ + GCNE composite. Different groups were placed in a 37 °C incubator and their dissolved oxygen content was measured at different time points. Photographs of bubble production were taken after adding 30% H$_2$O$_2$ into the pre-warmed GCNC hydrogel complex.

3.4. Verification of H⁺ adsorption by chitosan

In order to verify the adsorption of chitosan on H^+, pH measurement and solubility observations were carried out. At 37 °C, the samples and glucose were dissolved in PBS, and chitosan was added to the experimental group, the final concentrations of Glu, GCNE composite and chitosan were 3 mg ml^{-1}, 25 μg ml^{-1}, and 2 mg ml^{-1}, respectively. The pH values of the three groups at different time points were detected.

3.5. Cell culture

Human umbilical vein endothelial cells (HUVECs), and L929 cells were kindly obtained from the School of Pharmaceutical Sciences, Xiamen University. HUVECs were incubated in ECM containing 5% FBS, 1% endothelial cell growth supplement, and 1% penicillin–streptomycin. L929 cells were incubated in DMEM supplemented with 10% FBS in the incubator at 37 °C and 5% CO_2.

3.6. Cytotoxicity assay

L929 cells and HUVECs were seeded in 96-well plates at an initial cell density of 1.0×10^4 cells per well and incubated overnight. Afterward, different concentrations of the GCNE composite were incubated with the cells for 24 h. Then, the medium was replaced with MTT dissolved in a serum-free medium and incubated for 4 h. Finally, cell viabilities were quantified by an absorbance microplate reader (CMAX PLUS, Molecular Devices, USA) with the UV absorption at 490 nm. As for the hydrogel test, the L929 cells and HUVECs were seeded at a density of 1.0×10^4 cells per well into the lower chamber of a 24-well transwell plate with 8 μm pore-sized filter inserts (LABSELECT, 14341), overnight. Then, different concentrations of the GCNE composite were added to the 5% w/v chitosan-based hydrogel (GCNC hydrogel complex: 0, 10, 25, 50 μg ml^{-1}) and the gels were pre-added in the inserts to gel at 37 °C. The inserts were added to the lower chamber for 24 h co-incubation. Next, the cell viability of L929 and HUVEC was tested by MTT assay, which was mentioned above.

3.7. Intracellular ROS (H_2O_2) depletion and O_2 evaluation assay

L929 cells were used to evaluate the intracellular ROS scavenge and O_2 generation ability of the GCNE composite. For the ROS depletion assay, L929 cells were seeded in 48 well plates, overnight, and incubated with FBS-free DMEM and GCNE composite (10 μg ml^{-1} in FBS-free DMEM). After 24 h of incubation, cells were incubated with DCFH-DA (10 μM in FBS-free DMEM) for 20 min. Then, the fluorescence was detected using an inverted fluorescence microscope (Dmi8, Leica, Germany) and quantified by ImageJ software. For intracellular O_2 evaluation, L929 cells were seeded in a 48-well plate overnight and incubated with H_2O_2 (100 μM in FBS-free DMEM) and H_2O_2 + GCNE composite (10 μg ml^{-1} in FBS-free DMEM) for 6 h. Then, the cells were incubated with $[Ru(dpp)_3]Cl_2$ (10 μg ml^{-1}) for another 12 h and rinsed with PBS three times to remove free $[Ru(dpp)_3]Cl_2$. Then, the fluorescence was detected using

an inverted fluorescence microscope (Dmi8, Leica, Germany) and quantified using ImageJ software.

3.8. Cell proliferation assay

CFSE (5(6)-carboxyfluorescein diacetate succinimidyl ester; MCE) was used for visualization of cell proliferation *in vitro*, L929 cells and HUVECs were plated at a density of 5×10^4 per well into 24-well plates and treated with H_2O_2 (50 μM) for 12 h, then, they were washed several times and 1/10 medium volume of CFSE working solution (50 μM) was added to each well and incubate for 20 min. After washing several times to remove CFSE with PBS, the cells were treated with the GCNE composite solution (dilute with medium) and the solution was changed every 12 h to prevent toxicity caused by long-term acidity (and the control group was given the corresponding medium). At different time points (0 h, 12 h, 24 h, 48 h, 72 h), the fluorescence intensity of the cells was observed and photographed under an inverted fluorescence microscope (Dmi8, Leica, Germany) and quantified using ImageJ software.

3.9. Cell migration assay

L929 cells and HUVECs were seeded in 6-well plates at a density of 5×10^5 per well. After 24 h, cells filled every well. A micro-injury was created using sterile 10 μl pipette tips and washed with PBS. Then, the attached cells were treated with H_2O_2 (50 μM) for 12 h. After that, cells were treated with the GCNE composite (10 μg ml^{-1}), and the control group was treated with a serum-free medium. The cells were photographed at 0, 4, and 12 h after wounding using the inverted fluorescence microscope. The wound area was quantified using ImageJ software to evaluate the migration rate.

3.10. Tube formation assay

For the tube formation assay, pre-cooled Matrigel was added to the 24-well plates with 250 μl per well and incubated for 30 min at 37 °C to solidify the Matrigel. Afterward, HUVECs were seeded into the Matrigel-coated 24-well plates with 5×10^4 per well and treated with GCNE composite (10 μg ml^{-1}) and H_2O_2 (50 μM) for 4 h (and the control group was treated with serum-free medium). The tube formation was photographed under an inverted fluorescence microscope and quantified using ImageJ software.

3.11. *In vitro* antibiotic activity of chitosan-based hydrogel

Gram-negative *Escherichia coli* (*E. coli*) and Gram-positive *Staphylococcus aureus* (*S. A*) were employed to evaluate the antibiotic activity of the chitosan-based hydrogel (chitosan-*g*-poly (*N*-isopropylacrylamide) [CS-*g*-PNIPAAM]), which had been synthesized in our previous study and treated with the following process: prepare 5% (w/v) solution with acetic acid–sodium acetate buffer (pH 6.0; Sigma) in an ice bath and store at 4 °C overnight. The bacterial suspension (100 μl, 10^6 CFU ml^{-1}) was resuspended in a 10 ml sterilized Luria–Bertani (LB) medium. The thermo-sensitive solution was added to a 96-well plate to fill the bottom and the plate was maintained at 37 °C to form the hydrogel. Then, 150 μl of the above-mentioned suspension

was added to each well. The LB medium was used as a control and the experimental group was divided into the Glu, Glu + GCNE composite, Glu + hydrogel, and Glu + GCNE composite. The final concentrations of the Glu, GCNE composite and hydrogel were 3 mg ml^{-1}, 10 µg ml^{-1}, and 5% w/v. After that, the 96-well plate was fixed in an incubator at 37 °C with a relative humidity of not less than 90% and thoroughly shaken for 16 h. Finally, the absorbance of each well was measured at 600 nm.

For the visualization of antibacterial activity, 100 µl suspension was taken from a 96-well plate and diluted 100 times with the LB medium. Then, the diluted suspension was plated on an LB agar surface uniformly coated with *E. coli* (100 µl, 10^6 CFU ml^{-1}) and *S. A* (100 µl, 10^6 CFU ml^{-1}) for 18 h. Viable bacteria were observed and imaged.

3.12. Animals and diabetic models

Sprague-Dawley (SD) rats (180–220 g) were obtained from Xiamen University Laboratory Animal Center and all animal experiments were approved by the Animal Management and Ethics Committee of Xiamen University (XMULAC20210054). After a week of observation, the SD rats were used in the experiment.

For the establishment of the Type 1 diabetes model, SD rats were given a single intraperitoneal injection of streptozotocin (STZ) (50 mg kg^{-1}; Yeasen), which was dissolved in sterile citrate buffer (pH 4.2–4.5). After 2 days, the blood glucose of the rat tail vein was measured using a blood glucose meter, and the unqualified rats were supplemented with STZ (30 mg ml^{-1}). Seven days later, the blood glucose of rats was measured again and rats with a plasma glucose level of higher than 16.7 mmol L^{-1} were considered diabetic. The animals were maintained in a diabetic state throughout the wound healing process.

3.13. Chronic wound establishing, infecting, and healing

The diabetic rat *S. A*-infected cutaneous wound model was used to evaluate the chronic wound healing effect of the GCNC hydrogel complex. In brief, the SD rats were anesthetized with 10% chloral hydrate (3 ml kg^{-1}; MACKLIN) and shaved on their back. A round full-thickness cutaneous wound (9 mm × 9 mm) area was created on the back, after which, 50 µl of the *S. A* solution (10^7 CFU ml^{-1}) was dropped onto the wound. When the wound was made, blood from the wound was collected and blood glucose was measured. The diabetic rats were randomly divided into 5 groups ($n = 15$) including (1) 50 µl PBS without *S. A* infected as control; (2) 50 µl PBS; (3) 50 µl chitosan hydrogel (5% w/v); (4) 50 µl GCNE composite solution (25 µg ml^{-1}); (5) 50 µl GCNE composite (25 µg ml^{-1}) + chitosan–hydrogel (5% w/v). In addition, another two groups of healthy SD rats were made to explore the function of the GCNE composite, which included: (1) 50 µl PBS; (2) 50 µl GCNE composite solution (25 µg ml^{-1}). Afterward, the rats were individually separated in cages and their dressings were changed every other day. The weight and blood glucose levels were monitored at different time points. Before dropping the experimental solu-

tion onto the wound surface, all the rats were anesthetized. In order to monitor the wound healing process, a digital camera and a caliper were used to measure, and photograph wounds every other day. The equation used for calculating was;

$$\text{The wound size decrease rate} = (\text{wound area at day 0} - \text{wound area at certain day})/\text{wound area at day 0}.$$

All the rats were sacrificed on day 14, while the healing skins and organs were extracted for the next step. *In vivo* antibacterial experiments were carried out using skin tissue homogenate. In brief, the skin tissue was weighed and 10 times the volume of PBS solution was added and homogenized in a tissue homogenizer for 5 min. The supernatant was taken and diluted 10–1000 times. 100 µl of tissue abrasive was coated on an LB plate. Colonies formed after incubation at 37 °C for 12 h were counted.

3.14. Histological analysis

For histological analysis, tissues from the skin (day 14), heart, liver, spleen, lung, and kidney were harvested and soaked in 15% and 30% sucrose solution for 24 h and 12 h, respectively. Thereafter, tissue sections were embedded in an optimal cutting temperature (OCT) compound and sliced into tissue sections with a thickness of 6 µm by using a freeze slicer (CM1900, Leica, Germany). Then, they were stained with hematoxylin & eosin (H&E) and Masson's Trichrome stain kit (Solarbio) for observation and analysis under a microscope.

3.15. Immunofluorescence staining

After dehydration, skin tissue samples were made into frozen slices for fluorescence immunostaining. After being fixed with ice-cold acetone, the slice was rinsed in PBS and then blocked with a 5% Bovine Serum Albumin (BSA) blocking solution for 1 h. To evaluate the blood vessels, after 14 days of treatment, the skin slice was incubated with the PE anti-mouse CD31 Antibody (1 : 100; BioLegend, 102407) and dihydroethidium (DHE) (1 : 500) at 4 °C for 12 h. Afterward, the sections were washed several times with PBS to remove the staining solution. Finally, the sections were stained with DAPI-containing sealant and imaged with an inverted fluorescence microscope. The fluorescence intensity was quantified using the ImageJ software.

3.16. Statistical analysis

All experimental data and plots were calculated using Graphpad Prism 8.0. All data were presented as mean ± standard deviation (SD), and the difference between the two groups was studied using the Student's *t*-test. The *P*-value below 0.05 was considered statistically significant differences when *$P < 0.05$, **$P < 0.01$, and ***$P < 0.001$ *versus* the indicated group.

4. Conclusion

We successfully designed and prepared a multifunctional GOx–CAT nanoenzyme–chitosan (GCNC) hydrogel complex

with advanced functions of antibacterial, rapid hemostasis, blood sugar regulation, anti-inflammatory, and continuous oxygen supply for diabetic wound healing applications. Through the high-efficiency cascade effect of GOx and CAT in the nanostructure, the system can effectively regulate the blood glucose concentration of diabetic wounds, improve the wound's oxidative micro-environment, and continuously generate oxygen to promote cell proliferation, migration, and angiogenesis, which promoted diabetic wound healing. In addition, the temperature-sensitive chitosan hydrogel can quickly stop bleeding from the wound, and the chitosan can be activated by the product of GOx catalyzed glucose (gluconic acid) to enhance the antibacterial ability, preventing bacterial infection from worsening the wound surface, thereby effectively reducing the pain of diabetic patients and increasing their compliance and tolerance. This highly efficient enzyme cascade system with good biocompatibility can also be used for other tissue injuries related to diabetes. We believe this multifunctional GCNC hydrogel complex will have a wide range of applications in translational medicine and regenerative medicine, such as organ transplantation and regeneration, or surgical tissue repair.

Conflicts of interest

There are no conflicts to declare.

Acknowledgements

References

1 E. W. Gregg, Y. J. Cheng, M. Srinivasan, J. Lin, L. S. Geiss, A. L. Albright and G. Imperatore, *Lancet*, 2018, **391**, 2430–2440.

2 P. Kazemian, F. M. Shebl, N. McCann, R. P. Walensky and D. J. Wexler, *JAMA Intern. Med.*, 2019, **179**, 1376–1385.

3 S. Dekoninck and C. Blanpain, *Nat. Cell Biol.*, 2019, **21**, 18–24.

4 G. C. Gurtner, S. Werner, Y. Barrandon and M. T. Longaker, *Nature*, 2008, **453**, 314–321.

5 Q. Ou, S. Zhang, C. Fu, L. Yu, P. Xin, Z. Gu, Z. Cao, J. Wu and Y. Wang, *J. Nanobiotechnol.*, 2021, **19**, 237.

6 V. Falanga, *Lancet*, 2005, **366**, 1736–1743.

7 S. A. Shah, M. Sohail, S. Khan, M. U. Minhas, M. de Matas, V. Sikstone, Z. Hussain, M. Abbasi and M. Kousar, *Int. J. Biol. Macromol.*, 2019, **139**, 975–993.

8 Z. Xu, B. Liang, J. Tian and J. Wu, *Biomater. Sci.*, 2021, **9**, 4388–4409.

9 G. Liu, Z. Bao and J. Wu, *Chin. Chem. Lett.*, 2020, **31**, 1817–1821.

10 S. Schreml, R. M. Szeimies, L. Prantl, S. Karrer, M. Landthaler and P. Babilas, *Br. J. Dermatol.*, 2010, **163**, 257–268.

11 C. K. Sen, *Wound Repair Regener.*, 2009, **17**, 1–18.

12 R. P. Wunderlich, E. J. Peters and L. A. Lavery, *Diabetes Care*, 2000, **23**, 1551.

13 S. Suvarnapathaki, X. Wu, D. Lantigua, M. A. Nguyen and G. Camci-Unal, *NPG Asia Mater.*, 2019, **11**, 65.

14 R. M. Stoekenbroek, T. B. Santema, D. A. Legemate, D. T. Ubbink, A. van den Brink and M. J. W. Koelemay, *Eur. J. Vasc. Endovasc. Surg.*, 2014, **47**, 647–655.

15 R. C. Lalieu, R. J. Brouwer, D. T. Ubbink, R. Hoencamp, R. Bol Raap and R. A. van Hulst, *Wound Repair Regener.*, 2020, **28**, 266–275.

16 D. N. Teguh, R. Bol Raap, A. Koole, B. Knippenberg, C. Smit, J. Oomen and R. A. van Hulst, *Wound Repair Regener.*, 2021, **29**, 254–260.

17 M. Heyboer, D. Sharma, W. Santiago and N. McCulloch, *Adv. Wound Care*, 2017, **6**, 210–224.

18 W. J. Ennis, E. T. Huang and H. Gordon, *Adv. Wound Care*, 2018, **7**, 397–407.

19 K. T. B. Santema, R. M. Stoekenbroek, M. J. W. Koelemay, J. A. Reekers, L. M. C. van Dortmont, A. Oomen, L. Smeets, J. J. Wever, D. A. Legemate and D. T. Ubbink, *Diabetes Care*, 2018, **41**, 112.

20 A. N. H. Hodges, J. S. Delaney, J. M. Lecomte, V. J. Lacroix and D. L. Montgomery, *Br. J. Sports Med.*, 2003, **37**, 516.

21 R. G. Frykberg, P. J. Franks, M. Edmonds, J. N. Brantley, L. Téot, T. Wild, M. G. Garoufalis, A. M. Lee, J. A. Thompson, G. Reach, C. R. Dove, K. Lachgar, D. Grotemeyer, S. C. Renton and T. W. O. S. G. on behalf of the, *Diabetes Care*, 2020, **43**, 616.

22 R. G. Frykberg, P. J. Franks, M. Edmonds, J. N. Brantley, L. Téot, T. Wild, M. G. Garoufalis, A. M. Lee, J. A. Thompson, G. Reach, C. R. Dove, K. Lachgar, D. Grotemeyer, S. C. Renton and o. b. o. t. T. S. Group, *Diabetes Care*, 2020, **43**, 616–624.

23 X. Zhang, G. Chen, Y. Liu, L. Sun, L. Sun and Y. Zhao, *ACS Nano*, 2020, **14**, 5901–5908.

24 Y. Li, R. Fu, Z. Duan, C. Zhu and D. Fan, *ACS Nano*, 2022, **16**, 7486–7502.

25 H. Chen, Y. Cheng, J. Tian, P. Yang, X. Zhang, Y. Chen, Y. Hu and J. Wu, *Sci. Adv.*, 2020, **6**, eaba4311.

26 Z. Zhu, L. Wang, Y. Peng, X. Chu, L. Zhou, Y. Jin, H. Guo, Q. Gao, J. Yang, X. Wang, Z. Long, Y. Ge, S. Lu and B. Wang, *Adv. Funct. Mater.*, 2022, 2201875.

27 Y. Liu, X. Zhao, C. Zhao, H. Zhang and Y. Zhao, *Small*, 2019, **15**, 1901254.

28 P. S. Patil, N. Fountas-Davis, H. Huang, M. Michelle Evancho-Chapman, J. A. Fulton, L. P. Shriver and N. D. Leipzig, *Acta Biomater.*, 2016, **36**, 164–174.

29 P. A. Shiekh, A. Singh and A. Kumar, *Biomaterials*, 2020, **249**, 120020.

30 H. S. Kim, X. Sun, J.-H. Lee, H.-W. Kim, X. Fu and K. W. Leong, *Adv. Drug Delivery Rev.*, 2019, **146**, 209–239.

31 A. Eming Sabine, P. Martin and M. Tomic-Canic, *Sci. Transl. Med.*, 2014, **6**, 265sr266.

32 Y. Sang, W. Li, H. Liu, L. Zhang, H. Wang, Z. Liu, J. Ren and X. Qu, *Adv. Funct. Mater.*, 2019, **29**, 1900518.

33 H. Wu, F. Li, W. Shao, J. Gao and D. Ling, *ACS Cent. Sci.*, 2019, **5**, 477–485.

34 Y. Peng, D. He, X. Ge, Y. Lu, Y. Chai, Y. Zhang, Z. Mao, G. Luo, J. Deng and Y. Zhang, *Bioact. Mater.*, 2021, **6**, 3109–3124.

35 Y. Zhou, C. Liu, Y. Yu, M. Yin, J. Sun, J. Huang, N. Chen, H. Wang, C. Fan and H. Song, *Adv. Mater.*, 2020, **32**, 2003708.

36 Z. Luo, L. Jiang, C. Xu, D. Kai, X. Fan, M. You, C. M. Hui, C. Wu, Y.-L. Wu and Z. Li, *Chem. Eng. J.*, 2021, **421**, 127725.

37 S. Wang, H. Zheng, L. Zhou, F. Cheng, Z. Liu, H. Zhang, L. Wang and Q. Zhang, *Nano Lett.*, 2020, **20**, 5149–5158.

38 M. Hu, K. Korschelt, P. Daniel, K. Landfester, W. Tremel and M. B. Bannwarth, *ACS Appl. Mater. Interfaces*, 2017, **9**, 38024–38031.

39 C. Tu, H. Lu, T. Zhou, W. Zhang, L. Deng, W. Cao, Z. Yang, Z. Wang, X. Wu, J. Ding, F. Xu and C. Gao, *Biomaterials*, 2022, **286**, 121597.

40 Y. Guan, H. Niu, Z. Liu, Y. Dang, J. Shen, M. Zayed, L. Ma and J. Guan, *Sci. Adv.*, 2021, **7**, eabj0153.

41 X. Cai, L. Jiao, H. Yan, Y. Wu, W. Gu, D. Du, Y. Lin and C. Zhu, *Mater. Today*, 2021, **44**, 211–228.

42 P. Wang, L. Peng, J. Lin, Y. Li, Q. Luo, S. Jiang, H. Tian, Y. Zhang, X. Liu and J. Liu, *Chem. Eng. J.*, 2021, **415**, 128901.

43 Y. Li, R. Fu, Z. Duan, C. Zhu and D. Fan, *Small*, 2022, **18**, 2200165.

44 X. Du, B. Jia, W. Wang, C. Zhang, X. Liu, Y. Qu, M. Zhao, W. Li, Y. Yang and Y.-Q. Li, *J. Nanobiotechnol.*, 2022, **20**, 12.

45 X. Yu, X. Fu, J. Yang, L. Chen, F. Leng, Z. Yang and C. Yu, *Mater. Today Bio*, 2022, **15**, 100308.

46 Y. Liang, J. He and B. Guo, *ACS Nano*, 2021, **15**, 12687–12722.

47 A. Maleki, J. He, S. Bochani, V. Nosrati, M.-A. Shahbazi and B. Guo, *ACS Nano*, 2021, **15**, 18895–18930.

48 G. Lokhande, J. K. Carrow, T. Thakur, J. R. Xavier, M. Parani, K. J. Bayless and A. K. Gaharwar, *Acta Biomater.*, 2018, **70**, 35–47.

49 Z. Xu, G. Liu, Q. Li and J. Wu, *Nano Res.*, 2022, **15**, 5305–5315.

50 Z. Luo, K. Xue, X. Zhang, J. Y. C. Lim, X. Lai, D. J. Young, Z.-X. Zhang, Y.-L. Wu and X. J. Loh, *Biomater. Sci.*, 2020, **8**, 1364–1379.

51 Z. Luo, X. Fan, Y. Chen, X. Lai, Z. Li, Y.-L. Wu and C. He, *Nanoscale*, 2021, **13**, 17737–17745.